

Nonequilibrium Bubbles in a Flowing Langmuir Monolayer

RM. Muruganathan,[†] Z. Khattari,[‡] and Th. M. Fischer^{*,†}

Department of Chemistry and Biochemistry, Florida State University, Tallahassee, Florida, and Institut fuer Röntgenphysik, Georg-August-Universitaet Göttingen, Germany

Received: July 8, 2005; In Final Form: September 8, 2005

We investigate the nonequilibrium behavior of two-dimensional gas bubbles in Langmuir monolayers. A cavitation bubble is induced in liquid expanded phase by locally heating a Langmuir monolayer with an IR-laser. At low IR-laser power the cavitation bubble is immersed in quiescent liquid expanded monolayer. At higher IR-laser power thermo capillary flow around the laser-induced cavitation bubble sets in. The thermo capillary flow is caused by a temperature dependence of the gas/liquid line tension. The slope of the line tension with temperature is determined by measuring the thermo capillary flow velocity. Thermodynamically stable satellite bubbles are generated by increasing the surface area of the monolayer. Those satellite bubbles collide with the cavitation bubble. Upon collision the satellite bubbles either coalesce with the cavitation bubble or slide past the cavitation bubble. Moreover we show that the satellite bubbles can also be produced by the emission from the laser-induced cavitation bubbles.

1. Introduction

The stability and coarsening of foams is of major relevance in food preparation, flotation, fire fighting, or enhanced oil recovery. Foams essentially consist of a collection of air bubbles separated by a negligible amount of fluid facets that meet in *Plateau borders*. Our understanding of foam rheology is still quite rudimentary. For this reason rheological properties of two-dimensional (2-D) model foams are the focus of several research groups.^{1–11} Due to the simplicity in visualizing, 2-D foams in Langmuir monolayers have become one of the model systems where theoretical predictions can be tested by simple experiments.

The rheology of 2-D foams reveals the nature of the foam flow when being subject to external stress. Mechanical gradients such as the gradients in the interfacial tension result in thermodynamic potential gradients that give rise not only to material transfer but also to the exchange of entropy in the foam. Hence the flowing foams are out of mechanical and thermal equilibrium. A single foam bubble that is out of mechanical and thermal equilibrium is a good model system to understand aspects of the rheology of entire foams.

The focus of this work is therefore to study individual two-dimensional model gas bubbles in a Langmuir monolayer that are out of mechanical and thermal equilibrium. In previous work¹² we have shown that a 2-D gas bubble can be mechanically pinned to a defined region of the monolayer by laser-induced cavitation in a liquid expanded surrounding. Here we use such a laser-induced cavitation bubble pinned to the focus of an IR-laser to study the behavior of individual gas bubbles in thermal gradients as well as the interaction with other gas bubbles. The induced gas bubble is surrounded by a liquid expanded phase and satellite gas bubbles that thermodynamically

coexist at the local surface pressure and temperature chosen for the experiment. The laser causes thermal gradients that induce thermo capillary flow of the surrounding monolayer around the pinned gas bubble. In this work we give a quantitative analysis for the thermo capillary flow in 2-D-monolayers. The satellite gas bubbles collide with the laser-induced gas bubble. Bubble collisions allow the investigation of processes such as the sliding of one bubble over the other, the replacement of one bubble by the other, and topological transitions in the bubbly liquid. Moreover, the laser heating gives rise to nonlinear processes such as nonstationary bubble shapes with intermittent emission of satellite bubbles. Such nonlinear processes also occur in sheared foams. The observed processes and the quantified results given in this paper are therefore essential for the understanding of the rheological behavior of two-dimensional monolayer foams.

2. Experimental Section

2.1 Setup. Our setup consists of a home-built Langmuir trough with a fluorescence microscope that works with a 100× water immersion objective, numerical aperture 1.0, built into the bottom of the temperature-controlled film balance. The same objective is used to focus an IR-laser beam ($\lambda = 1064$ nm, $P = 10$ mW – 4 W) onto the central imaging region of the monolayer. The main purpose of this laser is to locally heat the monolayer by the absorption of the IR-light by the water (absorption coefficient of water at $\lambda = 1064$ nm: $\alpha \approx 0.1$ cm⁻¹). The setup has been described in detail elsewhere¹³ and we have made use of the laser heating previously to visualize cavitation,^{12,14} local phase transitions,¹⁵ and local collapse¹⁶ in monolayers.

Quantifying the Laser Heating. The applied laser power P (10 mW – 4 W) causes an observable local heating. This can melt the low-temperature phase in a locally defined region ($10 \mu\text{m} \leq r \leq 100 \mu\text{m}$). In the beam waist of the laser, a fraction of 10^{-6} of the laser power P is converted into heat. Assuming

* Corresponding author e-mail: tfischer@chem.fsu.edu.

[†] Florida State University.

[‡] Georg-August-Universitaet Göttingen.

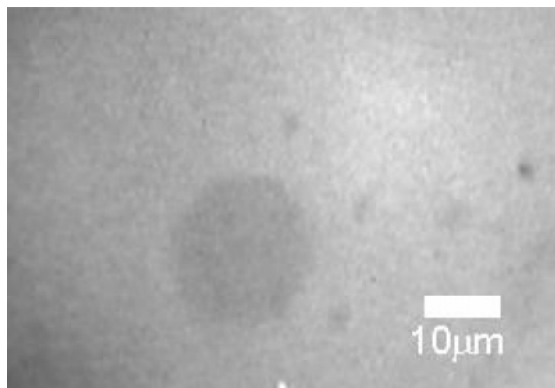


Figure 1. Laser-generated gas bubble at an IR laser power of $P = 1.2$ W in liquid expanded phase of methyloctadecanoate labeled with 0.8% of fluorescence dye (BODYPY), $T = 37$ °C, $A = 35$ Å²/molecule.

this heat is dissipated into the subphase by heat conduction only, the rise in temperature within the focus is estimated to be

$$\Delta T = \alpha \frac{3P}{4\pi\kappa} \quad (1)$$

Here, $\kappa \approx 0.6$ W/m·K is the heat conductivity of water. Equation 1 predicts that applying 1 W of laser power creates the local temperature difference of $\Delta T \approx 5$ K.

2.2 Fatty Acid Methyl Ester Monolayer. Methyloctadecanoate from ICN Biomedicals, Inc. Germany (claimed to be 99+% pure) has been used without further purification. BODYPY-FL C₁₆, used as a fluorescent dye, was purchased from Molecular Probes, USA. Dimyristoylphosphatidylcholine (DMPC) and Dihydrocholesterol (Dchol) from Avanti Polar Lipids (Alabaster, AL) claimed to be 99+% pure has been used without further purification. Nitrobenzoxadiazol-hexadecylamine (NBD-HDA), used as a fluorescent dye, was purchased from Molecular Probes, USA. Surfactant solution containing 0.8% of fluorescent dye was spread from chloroform (p.a. Fisher) onto pure water (Millipore Milli-Q at 18 MΩ) contained in the Teflon trough. Experiments were performed between 23 and 42 °C.

3. Results and Discussion

a. Cavitation Bubble in a Quiescent Liquid Expanded Phase. Figure 1 shows a laser-induced cavitation bubble of radius $R \approx 8$ μm in a methyloctadecanoate monolayer at an external temperature of $T_\infty = 37$ °C, the area per molecule $A \approx 35$ Å²/molecule, and a laser power of $P = 1.2$ W. In previous work,¹⁴ we have shown that the cavitation bubble arises due to thermal Marangoni stress leading to a convection roll that opens the bubble. We estimated the cavitation bubble radius as

$$R \approx -\frac{d\sigma_w}{dT} \frac{\alpha r_F P}{\kappa(\pi_\infty - \pi_b) \left(\frac{D(\pi_\infty - \pi_b)}{\beta E} + 1 \right)} \quad (2)$$

Here $d\sigma_w/dT$ is the slope of the surface tension of water with temperature, r_F is the focal width of the laser focus, π_b is the binodal surface pressure of the liquid expanded/gas coexistence, D and E are the diffusion constant and Gibb's elasticity of the gaseous phase, respectively, and β is the temperature diffusivity of water. Note that this equation predicts the cavitation bubble radius to increase as the external pressure is lowered toward the binodal pressure. The closer one is to liquid expanded gas coexistence the larger the cavitation bubble will be. The cavitation bubble in Figure 1 is far from the coexistence region,

and the radius is small. No flow other than always-present air-convection-driven flow is observed in the liquid expanded phase at these conditions.

b. Thermo Capillary Flow Past the Cavitation Bubble.

The situation changes when further increasing the laser power or if we lower the external surface pressure closer to the binodal pressure (expand the monolayer). A stationary convective flow in an arbitrary direction breaks the radial symmetry of the flow pattern. The convective flow causes the laser-induced cavitation bubble to be displaced from the laser focus further downstream by a distance d . We could measure the flow profile of this convective flow by simply increasing the laser power. Increasing the IR laser power results in the formation of smaller satellite bubbles around the cavitation bubble; these satellite bubbles move along the monolayer. We then track the motion of the smaller gas bubbles that move around the laser-induced cavitation bubble. This way of tracking the monolayer flow, however, is accompanied by large distortions of the laser-induced cavitation bubble due to the high Peclet number: $Pe = \eta R^2 \gamma / \lambda$ (η the viscosity of the subphase, γ is the shear rate, and λ is the line tension between the gaseous and the liquid expanded phase).

Less deformation of the cavitation bubble is observed when using liquid domains in a coexistence region between two liquid phases in a mixed monolayer for the tracking of the motion. This is done in a monolayer mixture of 58% DMPC, 40% dihydrocholesterol, and 2% NBD-HDA at $T_\infty = 23$ °C, $A = 200$ Å²/molecule. Figure 2 shows an overlay of 7 images separated by a time of 80 ms of this mixture exposed to an IR laser of $P = 2$ W.

The symmetry breaking flow around the laser-induced cavitation bubble is from the left toward the right and dihydrocholesterol rich domains are swept along the streamlines of the flow. The laser-induced cavitation bubble is circular with the exception of the rear of the bubble which is deformed toward a streamlined shape.

Breaking of the radial symmetry leads to a temperature gradient along the liquid expanded/gas-phase boundary of the laser-induced cavitation bubble. If the displacement d of the bubble from the laser center is small and assuming that the temperature profile around the laser is dominated by heat conduction we estimate the temperature gradient along the bubble boundary as

$$\frac{dT}{d\vartheta} = -\frac{\alpha P r_F d \sin \vartheta}{2\pi\kappa R^2} \quad (3)$$

We believe that this temperature gradient is the major source for the flow of the monolayer surrounding the laser-induced cavitation bubble. Since the line tension $\lambda(T)$ of the liquid expanded/gas-phase boundary depends on temperature, the temperature gradient will cause a line tension gradient

$$\frac{d\lambda}{d\vartheta} = \frac{d\lambda}{dT} \cdot \frac{dT}{d\vartheta} \quad (4)$$

that gives rise to thermo capillary flow. Similar flow is observed for three-dimensional bubbles that are immersed in a liquid with a linear temperature gradient.^{17–22} To estimate the monolayer flow caused by the thermal gradient we consider a 2-D circular gas bubble embedded in liquid surroundings subject to a thermal gradient. The 2-D-Marangoni flow that opens the laser-induced cavitation bubble effects only the flow inside the laser-induced cavitation bubble not the flow in the liquid expanded phase that we measure. Therefore, in our theoretical derivation we neglect the 2-D-Marangoni flow that superposes the thermo capillary

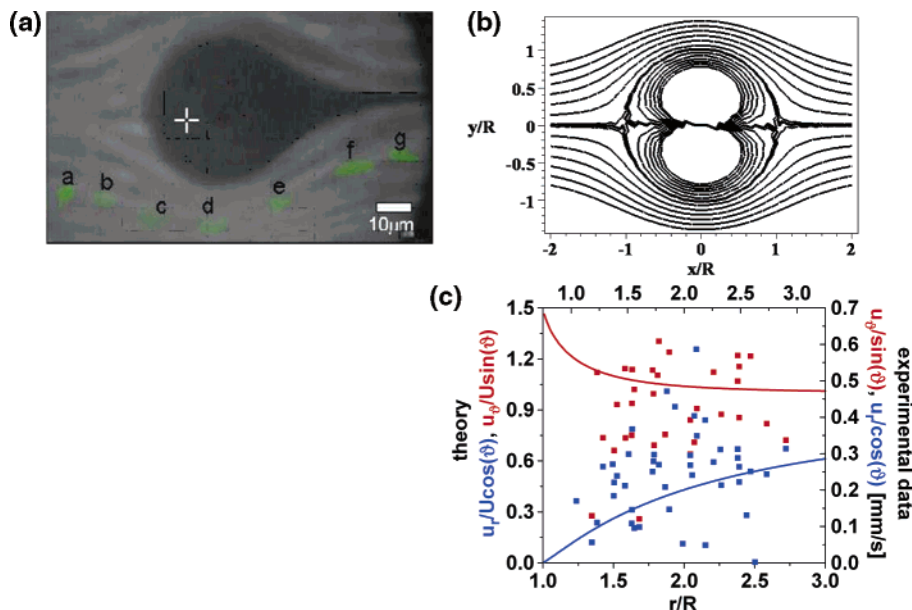


Figure 2. (a) Overlay of 7 fluorescence microscope images separated by 80 ms each of a DMPC/DChol mixture illuminated with an IR laser. The black streamline-shaped laser-induced cavitation bubble is marked with a cross hair that indicates the point where the laser is focused. One dihydrocholesterol rich domain has been marked in green (a–g) in each image so one can see the flow of this domain while time progresses. Video clip 1 (see Supporting Information) shows the motion of the DMPC/DChol liquid expanded mixture around the laser-induced cavitation bubble. (b) Theoretically predicted streamlines for a thermo capillary flow driven by a thermal gradient via the temperature dependence of the liquid gas line tension. (c) Normalized theoretical and experimental radial and azimuthal velocity profile plotted as a function of the normalized radial position. The theory predicts that the data should fall on this master curve for any azimuthal position. We extract a value of $U = 0.47$ mm/s for the thermo capillary velocity.

flow caused by the line tension gradient and just accept the presence of the bubble. Both the gaseous and the liquid expanded phase are 2-D-fluids of negligible surface shear viscosity.²³ Viscous dissipation therefore is governed by the flow of the 3-D subphase under the monolayer. A positive temperature-dependent line tension λ between the liquid and gaseous phase is associated with the phase boundary. Since the temperature varies as a function of the location at the surface so does the line tension. It is the velocity profile generated by the gradient in line tension that we wish to calculate. The flow of the subphase is described by Stokes equations and the continuity equation

$$-\nabla p + \eta \nabla^2 \mathbf{u} = 0 \quad \text{and} \quad \nabla \cdot \mathbf{u} = 0 \quad (5)$$

where p is the subphase pressure and \mathbf{u} denotes the subphase velocity. The general solution in a cylindrical coordinate system (r, ϑ, z) can be written as²⁴

$$\mathbf{u} = \nabla \Xi + \nabla(\mathbf{e}_z \Psi) + r \frac{\partial}{\partial r}(\nabla \Pi) + \mathbf{e}_z \frac{\partial \Pi}{\partial z} \quad \text{and} \quad p = -2\eta \frac{\partial^2 \Pi}{\partial z^2} \quad (6)$$

where Ξ, Ψ , and Π are scalar functions solving the Laplace equation

$$\nabla^2 \{\Xi, \Psi, \Pi\} = \{0, 0, 0\} \quad (7)$$

From the velocity boundary conditions $u_z(z=0) = 0$ and from the incompressibility of all monolayer phases $\nabla_s \cdot \mathbf{u}_s = 0$ (∇_s and \mathbf{u}_s are the surface gradient and the surface velocity) it follows that $\Pi = \Xi = 0$ and all streamlines are lying in planes parallel to the air–water interface. The remaining stream

function Ψ which is in accordance with the required symmetry is

$$\Psi(r, \vartheta, z) = 2UR \sin \vartheta \int_0^\infty dk k^{-1} a(kR) J_1(kr) e^{-kz} \quad (8)$$

where $a(kR)$ is a function of kR to be determined, $J_n(kr)$ is the Bessel function of order n and argument kr . Using eqs 8 and 6 we find

$$u_r(r, \vartheta, z) = U \cos \vartheta \int_0^\infty dk R a(kR) [J_2(kr) + J_0(kr)] e^{-kz}$$

$$u_\vartheta(r, \vartheta, z) = U \sin \vartheta \int_0^\infty dk R a(kR) [J_2(kr) - J_0(kr)] e^{-kz}$$

$$u_z(r, \vartheta, z) = 0$$

$$p(r, \vartheta, z) = \text{const} \quad (9)$$

The fluid motion of the liquid expanded and gaseous phase obeys the 2-D Stokes equation

$$-\nabla_s \pi_m + \eta \frac{\partial \mathbf{u}}{\partial z} - \frac{\lambda(\vartheta)}{R} \delta(r-R) \mathbf{e}_r = 0 \quad \text{for } z=0 \quad (10)$$

Here π_m is the surface pressure of the monolayer, ∇_s is the surface gradient, the second term is the viscous drag force from the subphase, and the last term ensures that the dynamic normal surface stress satisfies the Laplace condition. $\lambda(\vartheta)$ is the line tension of the liquid expanded–gaseous interface, and $\delta(r-R)$ is Dirac's delta function. Taking the surface curl of eq 10, which

eliminates the surface pressure, and insertion of eq 9 leads to the integral equation for $a(kR)$

$$\int_0^\infty dk 2\eta U \sin \vartheta k^2 a(kR) J_1(kr) = -\frac{1}{R^3} \frac{d\lambda}{d\vartheta} \delta(r - R) \quad (11)$$

The equation is solved by

$$a(kR) := A\delta(kR) - B \frac{J_1(kR)}{kR} \quad (12)$$

where A and B are constants. The requirement that $\mathbf{u}(r \rightarrow \infty) = U\mathbf{e}_x$ yields $A = 1$ while the impermeability of the bubble boundary $u_r(r = R) = 0$ yields $B = 3\pi/8$. Inserting eq 12 into eq 9 and using the constants A and B results in the surface velocity profile

$$u_r(z = 0) = U \cos \vartheta \begin{cases} 1 - \frac{1}{2}[K(r/R) - D(r/R) + E(r/R)] & \text{for } r < R \\ 1 - \frac{R}{2r}[K(R/r) - D(R/r) + E(R/r)] & \text{for } r > R \end{cases} \quad (13)$$

$$u_\vartheta(z = 0) = U \sin \vartheta \begin{cases} 1 - \frac{1}{2}[K(r/R) - D(r/R) - 2E(r/R)] & \text{for } r < R \\ 1 - \frac{R}{2r}[-2K(R/r) + 2D(R/r) + E(R/r)] & \text{for } r > R \end{cases}$$

where $K(k)$ and $E(k)$ are the complete elliptic integrals of the first and second kind,²⁵ and $D(k) = [K(k) - E(k)]/k^2$. Equation 13 therefore predicts the equatorial velocity to be $3/2U$, a factor of $3/2$ larger than the asymptotic velocity. The normalized radial and azimuthal velocity profiles eq 13 are plotted as a function of the normalized radius in Figure 2 (bottom right). We see that the data extracted from the images in Figure 2 top left follow the trend of the theoretical prediction, although with considerable scatter of data. (The scatter arises due to the high order of the velocity (mm/s) that forces us to measure the velocity by comparing two consecutive frames that are captured by the SIT-camera.)

The comparison of experiment and theory yields a thermo capillary velocity of $U = 0.47$ mm/s. The stream function ψ at the surface reads:

$$\psi(z = 0) = U \sin \vartheta \left[r - \frac{r^<}{2} \{K(r^</r^>) + D(r^</r^>) - E(r^</r^>)\} \right] \quad (14)$$

where

$$r^< = \min(r, R), \quad r^> = \max(r, R)$$

The streamlines of the surface flow are given by $\psi(z = 0) = \text{const}$ and they are displayed in Figure 2 top right. They correspond quite well to the streamlines seen in Figure 2. The relation between the thermo-capillary velocity U and the line tension gradient is found by inserting eq 12 into eq 11

$$U = \frac{4}{3\pi\eta R \sin \vartheta} \frac{d\lambda}{d\vartheta} \quad (15)$$

Combining the result in eq 15 with eqs 3 and 4 yields

$$\frac{d\lambda}{dT} = -\frac{3\pi^2\eta R^3 U \kappa}{2\alpha Pr_F d} \quad (16)$$

Using the experimental values and estimating $d \approx 1 \mu\text{m}$, eq 16 predicts a line tension gradient of $d\lambda/dT = 2.4$ pN/mK. The drag force onto the bubble is given by

$$F_{\text{drag}} = \oint \lambda \mathbf{e}_x d\vartheta = \oint \frac{3\pi\eta UR \cos^2 \vartheta}{4} \mathbf{e}_x d\vartheta = \frac{3\pi^2\eta UR}{4} \quad (17)$$

The drag force must be balanced by the pinning force of the laser for the bubble to remain in place. From eq 17 and the experimental data we estimate the pinning force to be of the order 4pN.

c. Deformations upon Collision. With increasing laser power the satellite bubbles surrounding the laser-induced cavitation bubble in methyloctadecanoate grow to almost the same size as the cavitation bubbles. The satellite bubbles do not behave as simple tracer particles and disturb the flow. When these larger satellite bubbles collide with the laser-induced cavitation bubble they cause a significant deformation of both the satellite and the cavitation bubble. One possibility is that the larger satellite bubble slides around the laser-induced cavitation bubble in an analogue way as the smaller satellite bubbles or dihydrocholesterol rich domains in the DMPC/DChol mixture. The only new effect is a deformation of both bubbles. However, for small impact parameters larger satellite bubbles can push the laser-induced cavitation bubbles out of the laser focus. As a result the former satellite gas bubble will finally be pinned by the laser; while the former laser-induced cavitation bubble is unpinned and leaves the collision region as a satellite bubble. The approaching satellite bubble may also coalesce with the laser-induced cavitation bubble.

Figure 3 ($T_\infty = 27^\circ\text{C}$, $A = 45 \text{ \AA}^2/\text{molecule}$, and $P = 1.6 \text{ W}$) shows a collision of a satellite gas bubble (bubble 1) with the laser-induced gas bubble (bubble 2) that leads to a switching of the roles of both bubbles. A small liquid expanded facet (blue arrows) forms between both bubbles as the satellite bubble reaches the laser pinned cavitation bubble ($t = 33$ ms). After the formation of the facet, the facet starts to move across the laser pinned cavitation bubble with its ends sliding on opposite sides of the laser pinned cavitation bubble ($t = 0-0.6$ s). Initially this facet motion is slow ($u_F = 40 \mu\text{m/s}$) and the facet almost comes to rest ($t < 0.4$ s). However, once ($t = 0.4$ s) the facet passes the equator of the laser pinned cavitation bubble and the laser focus (cross hair), the facet motion speeds up ($t = 429$ ms). The speeding up of the facet may be so violent that it leads to its rupture and the satellite and cavitation bubble coalesce. In other cases the facet remains intact and bubble 1 (the former satellite bubble) and bubble 2 (the former laser-induced cavitation bubble) switch roles. During this process bubble 1 increases its area to that of the laser pinned cavitation bubble while bubble 2 decreases its area; simultaneously the fast motion of the facet occurs ($t = 0.4-0.46$ s). Then the facet between the bubbles shortens quickly and the new satellite bubble shrinks and detaches from the new laser-induced cavitation bubble ($t > 0.46$ s). Finally, the new satellite bubble is swept along the thermo capillary flow and leaves the imaged region.

The fact that the sudden transition happens when the facet passes the focus of the laser indicates the transition to be governed by the interaction of the laser-induced convection inside the bubble and the facet. The laser convection inside the bubble generates a viscous stress on the facet that forces the

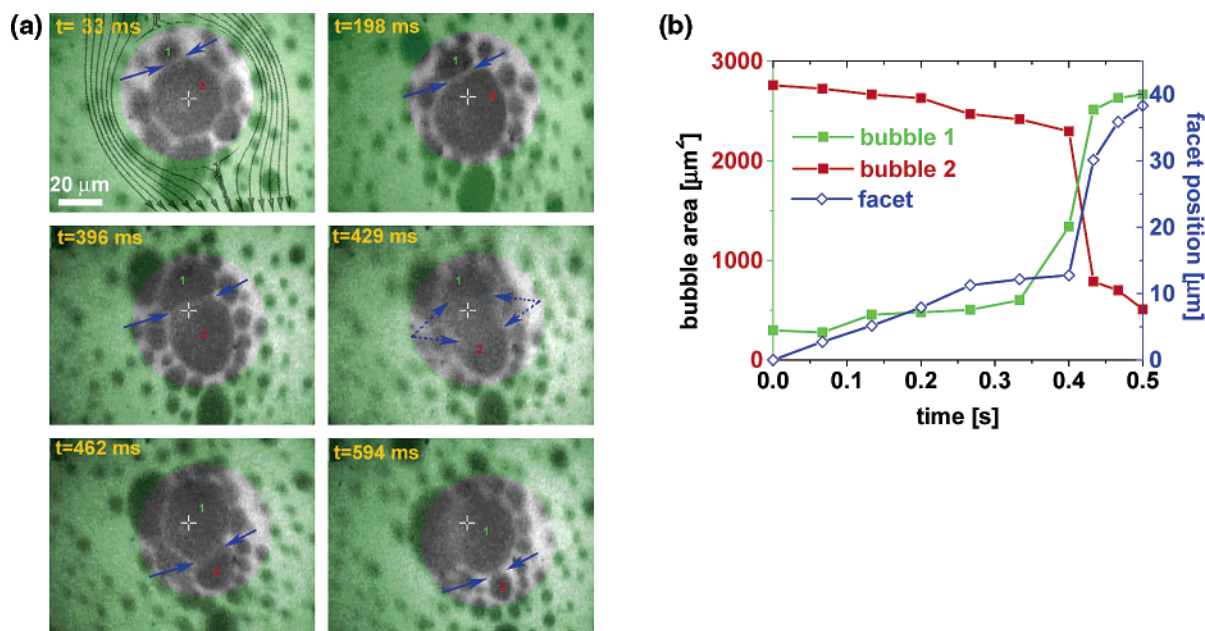


Figure 3. (a) Consecutive fluorescence microscopy images of gas bubbles in a liquid expanded phase in methyloctadecanoate Langmuir monolayer containing 0.8% of fluorescence dye (BODYPY), $T = 27^\circ\text{C}$. We have shaded the image green outside the collision area. The streamlines in the first image indicate the direction of the thermo capillary flow. Initially a laser-induced cavitation bubble (bubble 2) generated by the IR laser at 1.6 W is centered in the focus of the laser (cross hair). The sequence of images shows the consecutive change occurring while a satellite gas bubble (bubble 1) impacts on the laser induced cavitation bubble (2). The endpoints of the liquid expanded facet between both bubbles are marked by blue arrows. The areas of both bubbles are interchanged as the facet passes through the laser focus. In the fourth image ($t = 429$ ms) the movement of the facet is so fast that the facet appears smeared out over the range of its motion. Video clip 2 (Supporting Information) shows several consecutive bubble collision processes. (b) The dynamics of the area of both bubbles and the facet kinetics are strongly correlated showing that the replacement kinetics of the laser-induced cavitation bubble is governed by the facet passing the laser focus.

facet away from the laser. Initially the viscous drag from the thermo capillary flow of the liquid phase around both bubbles opposes the laser-induced cavitation pressure and both bubbles are pressed against each other leading to a slow motion of the facet caused by the unbalance of both viscous stresses. Once the facet passes the laser ($t > 0.43$ s) both forces act downstream. The bubbles are no longer pressed on to each other leading to a fast downstream motion of the facet. The former satellite bubble is converted into a laser-induced cavitation bubble that is pinned to the laser focus. The change of area of both bubbles (Figure 3 top right) corroborates this change in the nature of both bubbles. The former laser-induced cavitation bubble experiences no cavitation pressure after the facet passing the laser focus. It consequently shrinks and as it is no longer pinned to the laser leaves the collision area with the thermo capillary flow.

4. Bubble Emission

At elevated temperature and elevated laser power ($T_\infty = 42^\circ\text{C}$, $A = 50 \text{ \AA}^2/\text{molecule}$ and $P = 2.2$ W) the laser-induced cavitation bubble deforms before one creates satellite gas bubbles and there is a transition from a stationary to a nonstationary cavitation bubble. The nonstationary cavitation bubble (Figure 4 top left) exhibits an erratic motion of the bubble tail. The thermo capillary motion around the almost circular cavitation bubble leads to the formation of an elongated protrusion at the rear of the bubble. The length l of the protrusion increases ($t = 0\text{--}0.3$ s). The protrusion develops a neck connected to a thicker ellipsoidal shape that ends the protrusion ($t = 0.2$ s). After increasing in radius from $a = 1 \text{ }\mu\text{m}$ to $a = 5 \text{ }\mu\text{m}$ the ellipsoidal end breaks off the protrusion at the neck and forms a circular satellite gas bubble ($t = 0.4$ s). The satellite gas bubble is swept away by the thermo capillary flow, while the protrusion now having an end with significantly smaller

radius shortens, and eventually the shape of the cavitation bubble relaxes back to almost circular ($t > 0.4$ s). The entire process repeats as long as the laser power is on. While the length of the protrusion depends on the laser power, the average time between two satellite bubble break offs seems to be fairly independent of the applied laser power.

In the top right of Figure 4 we analyze a single event ($P = 2.2$ W and laser induced cavitation bubble radius $R = 18.8 \text{ }\mu\text{m}$) where a cavitation bubble elongates, emits a satellite bubble, and relaxes. We display the length of the protrusion as a function of time. The protrusion elongates for about half a second (open circles) and then the small bubble ($a = 5 \text{ }\mu\text{m}$) breaks off. The distance of the emitted bubble from the edge of the initially undeformed cavitation bubble increases (open squares) as the emitted bubble follows the thermo capillary flow. The filled circles indicate the relaxation process of the protrusion ending in a very small ellipsoidal shape after the break-off of the satellite bubble. The velocity of the elongating protrusion ending in the $a = 5 \text{ }\mu\text{m}$ ellipsoid was measured as $u_p = 149 \pm 5 \text{ }\mu\text{m}/\text{sec}$. It is smaller than the velocity of the thermo capillary flow measured by tracking the motion of the emitted satellite bubble, $u_\infty = 360 \pm 10 \text{ }\mu\text{m}/\text{sec}$. The relaxation velocity of the protrusion ending in a small ellipsoidal shape ($a = 1 \text{ }\mu\text{m}$) $u_p = -75 \pm 6 \text{ }\mu\text{m}/\text{sec}$. The motion of the protrusion can be understood by balancing the line tension with the hydrodynamic drag

$$2\lambda + \frac{3\pi^2}{4}\eta a(u_p - u_\infty) = 0 \quad (18)$$

Both measurements of elongation and relaxation are consistent with a line tension of $\lambda = 2.5$ pN. The entire process therefore happens because the drag of the thermo capillary flow is strong enough to pull out a protrusion that is thick enough. However,

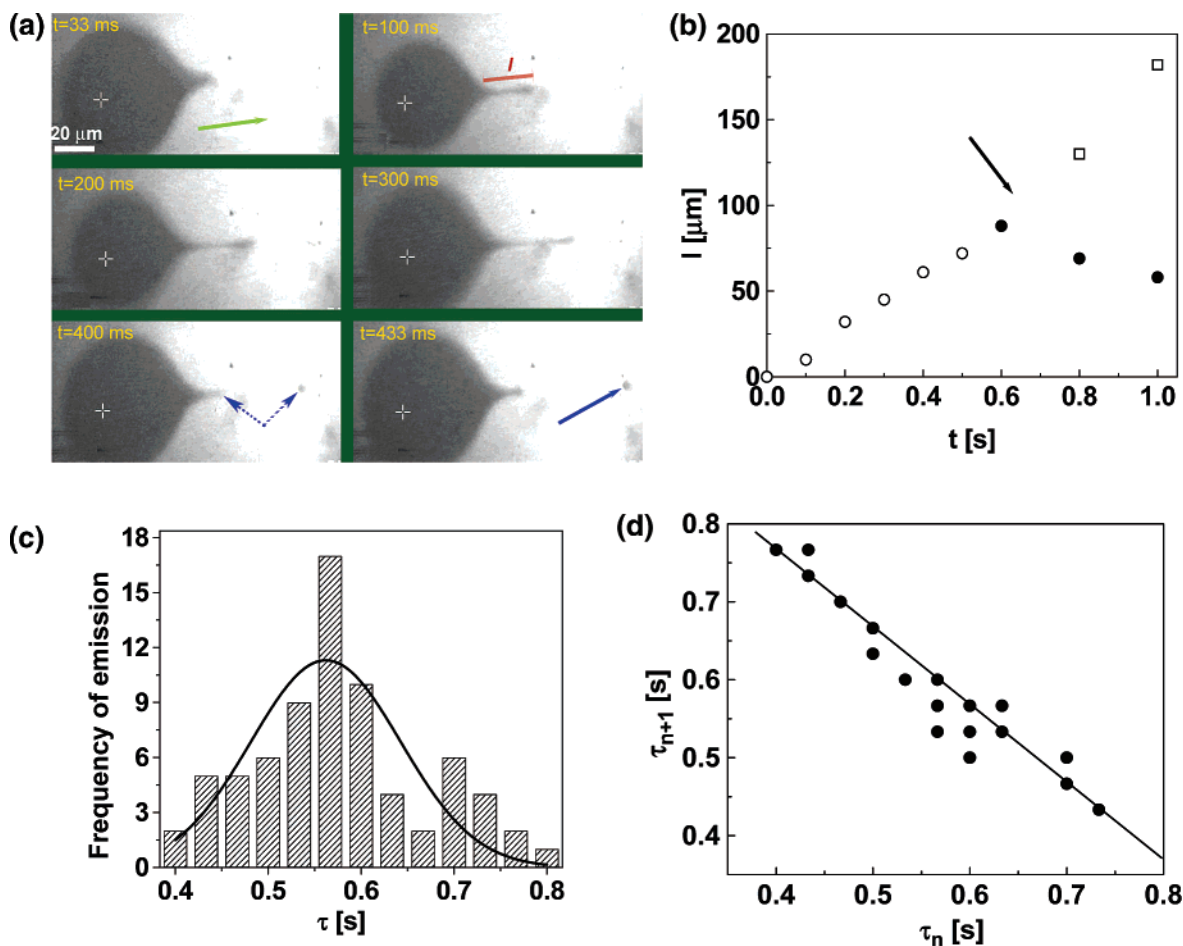


Figure 4. (a) Consecutive fluorescence microscopy images of the nonstationary shape of a laser-induced cavitation bubble in methyloctadecanoate ($T_{\infty} = 42^{\circ}\text{C}$, $A = 50 \text{ \AA}^2/\text{molecule}$) pinned by an IR laser (cross hair) of power $P = 2.2 \text{ W}$. The green arrow shows the direction of the thermo capillary flow. A protrusion at the rear of the bubble elongates until it ruptures ($t = 400 \text{ ms}$) and splits into a shortening protrusion and a small satellite bubble (blue arrows). Video clip 3 (Supporting Information) shows several consecutive cycles of the protrusion formation, satellite bubble emission, and retraction of the protrusion. (b) The length, l , of the protrusion and the distance of the emitted satellite bubble from the laser-induced cavitation bubble as a function of time. The break off of the satellite bubble is indicated by the blue arrow. (c) Distribution of bubble emission times, fitted by a Gaussian. (d) Plot of two successive emission times showing the deterministic chaotic behavior of the bubble emission.

when the protrusion is pulled out of the cavitation bubble there is no further supply of gas such that the protrusion thins everywhere but at the end. When the end breaks off, the drag on the smaller protrusion left behind is too weak to further elongate the droplet and the protrusion relaxes.

We followed the emission process of about 80 small satellite bubbles; all of them originate from the same laser-induced cavitation bubble and possess similar radius (about $5 \mu\text{m}$). The distribution of emission times (times from the start of elongation until the bubble emission) is displayed in the lower left of Figure 4. Among 80 emissions, more than 50% of the emissions occur between 0.5 and 0.6 s and we may fit the data with a Gaussian centered around $\tau = 0.56 \text{ s}$ of width 0.16 s. Subsequent emission times are negatively correlated. The lower right of Figure 4 shows a plot of the $(n + 1)$ th emission time versus the n th emission time. The data scatters around the line $\tau_{n+1} = 0.8s - \tau_n$. The emission of the $n + 1$ satellite bubble after the n th emission of a satellite bubble is not a random statistical process where τ_n and τ_{n+1} would be uncorrelated and statistically scatter around the average. In contrast, the next emission time is entirely determined by the preceding emission. The lower right of Figure 4 therefore is a clear proof that the bubble emission is a deterministic nonlinear not a random process.

Conclusions

Laser-induced cavitation bubbles arise due to thermal Marangoni stress producing a convection roll in the subphase that opens the bubble. Sufficient heating produces a thermo capillary flow. Gradients in temperature and a temperature-dependent line tension propel the liquid surroundings around the laser-induced cavitation bubble that is fixed in position. We could compare the experimental flow profile with theoretical predictions with satisfactory agreement. At even stronger laser power satellite laser bubbles surround the laser-induced cavitation bubble. The interaction of the satellite bubbles with the pinned bubble leads to a variety of phenomena including the replacement of the laser-induced cavitation bubble by satellite laser bubbles, the coalescence of bubbles, and the emission of satellite bubbles. The dynamics of bubble interaction is highly nonlinear but deterministic.

Supporting Information Available: Video clip 1 showing the thermocapillary motion of the DMPC/DChol liquid expanded mixture around the laser-induced cavitation bubble that is depicted in Figure 2; video clip 2 showing several consecutive bubble collision processes, one of which is depicted in Figure 3; video clip 3 showing a laser pinned cavitation bubble emitting several satellite bubbles; several consecutive cycles of the

protrusion formation, satellite bubble emission, and retraction of the protrusion are shown in the clip; one of these cycles is shown at different stages in Figure 4. This material is available free of charge via the Internet at <http://pubs.acs.org>.

References and Notes

- (1) Moore, B.; Knobler, C. M.; Broseta, D.; Rondelez, F. *J. Chem. Soc., Faraday Trans. 2* **1986**, 82 (10), 1753.
- (2) Kuz, V. A. *Phys. Rev. A* **1992**, 45, 8975.
- (3) Dennin, M.; Knobler, C. M. *Phys. Rev. Lett.* **1997**, 78, 2485.
- (4) el Kader, A. A.; Earnshaw, J. C. *Phys. Rev. Lett.* **1999**, 82, 2610.
- (5) Fortes, M. A.; Rosa, M. E. *J. Phys.: Condens. Matter* **1999**, 11, 7947.
- (6) Mann, E. K.; Primak, S. V. *Phys. Rev. Lett.* **1999**, 83, 5397.
- (7) Debregeas, G.; Tabuteau, H.; di Meglio, J. M. *Phys. Rev. Lett.* **2001**, 87, 178305.
- (8) Khaskova, T. N.; Kruglyakov, P. M. *Colloid J.* **2001**, 63, 476.
- (9) Vaz, M. F.; Fortes, M. A. *J. Phys.: Condens. Matter* **2001**, 13, 1395.
- (10) Courty, S.; Dollet, B.; Elias, F.; Heinig, P.; Graner, F. *Europhys. Lett.* **2003**, 64, 709.
- (11) Lauridsen, J.; Chanan, G.; Dennin, M. *Phys. Rev. Lett.* **2004**, 93, 018303.
- (12) Khattari, Z.; Steffen, P.; Fischer, Th. M.; Bruinsma, R. *Phys. Rev. E* **2002**, 65, 041603.
- (13) Wurlitzer, S.; Lautz, C.; Liley, M.; Duschl, C.; Fischer, Th. M. *J. Phys. Chem. B* **2001**, 105, 182.
- (14) Khattari, Z.; Hatta, E.; Kurth, D. G.; Fischer, Th. M. *J. Chem. Phys.* **2001**, 115, 9923.
- (15) Khattari, Z.; Fischer, Th. M. *J. Phys. Chem. B* **2004**, 108, 13696.
- (16) Muruganathan, R. M.; Fischer, Th. M. Laser induced local collapse in a Langmuir monolayer. *J. Phys. Chem. B* **2005** (in press).
- (17) Young, N. O.; Goldstein, J. S.; Block, M. J. *J. Fluid Mech.* **1959**, 6, 350.
- (18) Subramanian, R. S. *AIChE J.* **1981**, 27 (4), 646.
- (19) Bratukhin, Y. K. *Izv. Akad. Nauk. SSSR. Mekh. Zhidk. Gaza* **1975**, 5, 156; NASA Technical Translation NASA TT 17093 (June, 1976).
- (20) Chen, S. H. *J. Colloid Interface Sci.* **2000**, 230, 147.
- (21) Treuner, M.; Galindo, V.; Gerbeth, G.; Langbein, D.; Rath, H. J. *J. Colloid Interface Sci.* **1996**, 179, 114.
- (22) Harper, J. F. *Advances in Applied Mechanics*; Yih, C. S., Ed.; Academic Press: New York, 1972; Vol. 12, pp 59–129.
- (23) Steffen, P.; Heinig, P.; Wurlitzer, S.; Khattari, Z.; Fischer, Th. M. *J. Chem. Phys.* **2001**, 115, 994.
- (24) Happel, J.; Brenner, H. *Low Reynolds Number Hydrodynamics*; Martinus Nijhoff Publishers: The Hague, 1983; p 77.
- (25) Gradshteyn, L. S.; Ryzhik, I. M. *Table of Integrals, Series, and Products*, 6th ed.; Academic Press: San Diego, CA, 2000; p 8.112.